CLNS 11/2077
CLEO 11-04

Search for the decay $D_s^+ \to \omega e^+ \nu$

L. Martin,[1] A. Powell,[1] G. Wilkinson,[1] J. Y. Ge,[2] D. H. Miller,[2] I. P. J. Shipsey,[2] B. Xin,[2] G. S. Adams,[3] B. Moziak,[3] J. Napolitano,[3] K. M. Ecklund,[4] J. Insler,[5] H. Muramatsu,[5] C. S. Park,[5] L. J. Pearson,[5] E. H. Thorndike,[5] S. Ricciardi,[6] C. Thomas,[1,6] M. Artuso,[7] S. Blusk,[7] R. Mountain,[7] T. Skwarnicki,[7] S. Stone,[7] L. M. Zhang,[7] G. Bonvicini,[8] D. Cinabro,[8] A. Lincoln,[8] M. J. Smith,[8] P. Zhou,[8] J. Zhu,[8] P. Naik,[9] J. Rademacker,[9] D. M. Asner,[10,*] K. W. Edwards,[10] K. Randrianarivony,[10] G. Tatishvili,[10,*] R. A. Briere,[11] H. Vogel,[11] P. U. E. Onyisi,[12] J. L. Rosner,[12] J. P. Alexander,[13] D. G. Cassel,[13] S. Das,[13] R. Ehrlich,[13] L. Gibbons,[13] S. W. Gray,[13] D. L. Hartill,[13] B. K. Heltsley,[13] D. L. Kreinick,[13] V. E. Kuznetsov,[13] J. R. Patterson,[13] D. Peterson,[13] D. Riley,[13] A. Ryd,[13] A. J. Sadoff,[13] X. Shi,[13] W. M. Sun,[13] J. Yelton,[14] P. Rubin,[15] N. Lowrey,[16] S. Mehrabyan,[16] M. Selen,[16] J. Wiss,[16] J. Libby,[17] M. Kornicer,[18] R. E. Mitchell,[18] D. Besson,[19] T. K. Pedlar,[20] D. Cronin-Hennessy,[21] J. Hietala,[21] S. Dobbs,[22] Z. Metreveli,[22] K. K. Seth,[22] A. Tomaradze,[22] and T. Xiao[22]

(CLEO Collaboration)

[1] *University of Oxford, Oxford OX1 3RH, UK*
[2] *Purdue University, West Lafayette, Indiana 47907, USA*
[3] *Rensselaer Polytechnic Institute, Troy, New York 12180, USA*
[4] *Rice University, Houston, Texas 77005, USA*
[5] *University of Rochester, Rochester, New York 14627, USA*
[6] *STFC Rutherford Appleton Laboratory, Chilton, Didcot, Oxfordshire, OX11 0QX, UK*
[7] *Syracuse University, Syracuse, New York 13244, USA*
[8] *Wayne State University, Detroit, Michigan 48202, USA*
[9] *University of Bristol, Bristol BS8 1TL, UK*
[10] *Carleton University, Ottawa, Ontario, Canada K1S 5B6*
[11] *Carnegie Mellon University, Pittsburgh, Pennsylvania 15213, USA*
[12] *University of Chicago, Chicago, Illinois 60637, USA*
[13] *Cornell University, Ithaca, New York 14853, USA*
[14] *University of Florida, Gainesville, Florida 32611, USA*
[15] *George Mason University, Fairfax, Virginia 22030, USA*
[16] *University of Illinois, Urbana-Champaign, Illinois 61801, USA*
[17] *Indian Institute of Technology Madras, Chennai, Tamil Nadu 600036, India*
[18] *Indiana University, Bloomington, Indiana 47405, USA*
[19] *University of Kansas, Lawrence, Kansas 66045, USA*
[20] *Luther College, Decorah, Iowa 52101, USA*
[21] *University of Minnesota, Minneapolis, Minnesota 55455, USA*
[22] *Northwestern University, Evanston, Illinois 60208, USA*

(Dated: January 6, 2013)

arXiv:1105.2720v1 [hep-ex] 13 May 2011

Abstract

We present the first search for the decay $D_s^+ \to \omega e^+ \nu$ to test the four-quark content of the D_s^+ and the ω-ϕ mixing model for this decay. We use 586 pb^{-1} of e^+e^- collision data collected at a center-of-mass energy of 4170 MeV. We find no evidence of a signal, and set an upper limit on the branching fraction of $\mathcal{B}(D_s^+ \to \omega e^+ \nu)$ <0.20% at the 90% confidence level.

* Now at: Pacific Northwest National Laboratory, Richland, WA 99352

I. INTRODUCTION

Multiple observations of exotic charmonium states $[1-4]$ have been widely interpreted as four-quark states $[5-13]$. In this analysis we probe the four-quark content of the D_s^+ by searching for the decay $D_s^+ \to \omega e^+ \nu$ (charge conjugate states are implied throughout the article). Assuming that the ω is a pure two-quark state, its valence quarks are distinct from those of the D_s^+, and the decay can proceed through the diagram of Fig. 1, where the $(u\bar{u})$ or $(d\bar{d})$ come from within the D_s^+. The initial valence quarks annihilate while a lepton pair is produced. Neither Cabibbo-favored, nor Cabibbo-suppressed decays can contribute to this final state. The study of this specific process was first suggested in Ref. [14], and Ref. [15] estimates the theoretical branching fraction for the analogous decay $B^+ \to J/\psi\, \ell^+ \nu$.

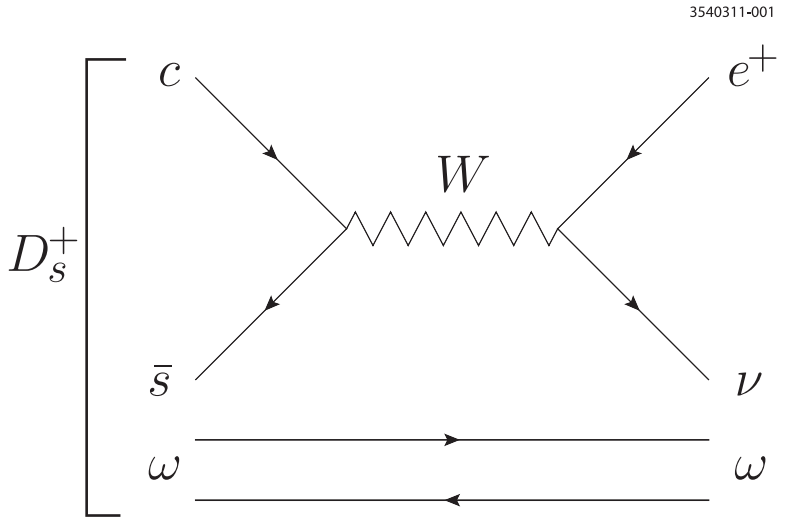

FIG. 1. Feynman diagram representing the four-quark semileptonic decay $D_s^+ \to \omega e^+ \nu$.

Recent work by Gronau and Rosner [16] concludes that any value of the branching fraction for $D_s^+ \to \omega e^+ \nu$ exceeding 2×10^{-4} is unlikely to be explainable by ω-ϕ mixing and would provide evidence for non-perturbative effects known as "weak annihilation" (see Ref. [16] for references). An estimate based on comparing hadronic and semileptonic processes gives a branching fraction of $(0.13 \pm 0.05)\%$. This is the first search for this decay mode.

We search for a positron candidate and an $\omega \to \pi^+\pi^-\pi^0$ candidate, which is the dominant decay mode with a branching fraction of 89.2% [17]. Cabibbo-favored decays exist in the same final state, $D_s^+ \to \eta e^+ \nu$ and $D_s^+ \to \phi e^+ \nu$, with $\mathcal{B}(\eta \to \pi^+\pi^-\pi^0)$ =22.73% and and $\mathcal{B}(\phi \to \pi^+\pi^-\pi^0)$ =15.32% [17]. They can play the role of control samples, which are used directly in the analysis in a variety of ways. For example, the effect of certain selection requirements can be readily estimated from any change in the η and ϕ populations. The two control samples are also well measured using the independent final states $\eta \to \gamma\gamma$ and $\phi \to K^+K^-$. Therefore, this analysis has good statistical sensitivity, and unusually strong control samples using CLEO-c data directly.

The remainder of this article is organized as follows. In Sec. II, the detector, data, and Monte Carlo (MC) samples are described. The data analysis method is described in Sec. III. The fitting procedure is described in Sec. IV. The determination of the branching fraction is discussed in Sec. V.

II. DETECTOR, DATA AND MC SAMPLES

The data used in the analysis are e^+e^- collisions at a center-of-mass energy $\sqrt{s}$ =4170 MeV. The data are collected by the CLEO-c detector and correspond to an integrated luminosity of 586 pb^{-1}, or 0.6×10^6 $D_s^+D_s^-$ inclusive pairs.

The CLEO-c detector is optimized for physics in the charmonium region and is described in detail in Ref. [19]. The tracking system consists of a central, low mass drift chamber, which wraps directly around the beam pipe, and a main drift chamber inside a solenoidal magnetic field. The particle identification system combines the track information from the gas chambers (dE/dx) and the associated ring-imaging Cherenkov detector (RICH) data. The electromagnetic calorimeter consists of CsI crystals, arranged in cylindrical fashion around the drift chamber, to make a barrel at angles given by $|\cos\theta| < 0.7$, with θ being the angle measured from the interaction point (IP) with respect to the beam axis. The ends of the cylinder are also instrumented with CsI crystals and are referred to as the end-cap regions.

MC simulations of the known physics processes [20] and of the CLEO-c detector [21] are used to estimate backgrounds and calculate signal resolution and efficiencies. The known charm physics processes are included in the $c\bar{c}$ MC simulation. All types of charm backgrounds, dominant in this analysis, are simulated to 20 times the statistics in the data, while the continuum (u, d, s) backgrounds are simulated to 6.6 times the statistics in the data. In the following, where MC results are presented, we multiply the continuum MC sample by 3 to obtain a consistent $\times 20$ normalization. By convention, $c\bar{c}$ MC refers to the charm part of the MC, continuum MC is the non-charm part, and MC is the weighted sum of the two.

The signal MC sample consists of 8×10^5 $D_s^+ \to \omega e^+\nu$ events generated according to phase space distribution. The same number of events was generated for the $D_s^+ \to \eta e^+\nu$ and $D_s^+ \to \phi e^+\nu$ control samples.

Further samples for dominant sources of backgrounds were generated. A sample of 2×10^5 $D_s^+ \to \omega\pi^+\pi^0$ events was separately generated, corresponding to about 23.5 times the number of such expected decays in the data. In addition, 5000 events (96 times the data) were generated for the decay chain $D_s^+ \to \eta' e^+\nu$ followed by $\eta' \to \omega\gamma$.

III. DATA SELECTION

About 95% of the $e^+e^- \to D_s^+X$ events are formed through the following exclusive reactions [18]

$$e^+e^- \to D_s^+D_s^{\star-} \text{ and } e^+e^- \to D_s^-D_s^{\star+}. \quad (1)$$

Equal amounts of positive and negative $D_s^\star$ states are produced, and about 95% of them decay to $D_s\gamma$. The analysis described here selects exclusively both final states in Eq. (1). In the following, we retain both events where the γ is associated with the positive side, the signal side due to the convention established in Sec. I, and where the γ is associated with the negative side, or tag side. Several kinematic constraints are available, but only those that select both reactions in Eq. (1) are used.

First we search for an exclusively reconstructed hadronic D_s^- candidate, the tag, and a photon candidate. Requiring both of these objects, with three kinematic selections applied, strongly suppresses the backgrounds. The photon candidate, and all tracks and showers which are daughters of the tag candidate, are not used when searching the rest of the

event, which, due to the exclusive nature of the analysis, must be the signal candidate. The following are required to form a signal candidate: a positron of opposite charge to the tag, precisely three charged tracks, a π^0 candidate, and net event charge equal to zero. Furthermore, the missing energy and momentum are required to be in a relation consistent with the presence of a nearly massless neutrino. Extra showers in the event are ignored.

The selection is described in detail in the remainder of this section.

A. Charged and neutral particles selection

The criteria for a good track include the requirements that its minimum distance to the IP does not exceed 5 mm in the plane perpendicular to the beam axis and 5 cm along the beam axis. Phase space is limited to $|\cos\theta| < 0.93$, with θ being the angle with the beam axis, and momentum 0.05 GeV $< p < 2$ GeV. Good tracks are then selected as pion or kaon using dE/dx and RICH data according to the algorithms described in detail in Ref. [22].

Photon candidates are contiguous groups of crystals recording significant energy deposition. They are required to be unmatched to tracks or noisy crystals, and to have a transverse profile consistent with expectations from an electromagnetic shower. The minimum cluster energy is 30 MeV.

Positrons are selected by requiring a good track, and the combined positron probability of the particle ID system and E/p (the ratio between the shower energy associated with the candidate electron and its track momentum) to be greater than 0.8. Positron phase space requirements are $|\cos\theta| < 0.9$ and $p > 0.2$ GeV.

π^0 and η candidates are selected by requiring a photon candidate in the barrel or endcap, with $|\cos\theta| < 0.93$. This photon is combined with a second photon, which must not be associated with a noisy crystal, and the invariant mass of the two photons must be within 3 standard deviations of the nominal π^0 and η masses [17].

K^0_S candidates are selected by requiring two oppositely charged tracks. If they are assigned the nominal π^+ mass [17], their invariant mass must be within 12 MeV of the nominal K^0_S mass [17]. A common vertex is calculated, and it is required to be radially displaced from the IP by at least 3 standard deviations.

TABLE I. Definitions of $M_{\rm tag}$ signal and sideband definitions for the tag modes.

Mode	Signal region (GeV)	Low sideband (GeV)	High sideband (GeV)
$K^0_S K^-$	[1.954, 1.983]	[1.910, 1.939]	[1.998, 2.026]
$K^+K^-\pi^-$	[1.954, 1.982]	[1.911, 1.940]	[1.996, 2.025]
$K^{\star-}\overline{K}^{\star 0}$	[1.953, 1.983]	[1.909, 1.938]	[1.997, 2.027]
$\pi^+\pi^-\pi^-$	[1.955, 1.982]	[1.913, 1.941]	[1.996, 2.024]
$\eta\pi^-$	[1.940, 2.001]	[1.892, 1.922]	[2.019, 2.050]
$\eta\rho^-$	[1.940, 1.998]	[1.885, 1.914]	[2.021, 2.050]
$\pi^-\eta'(\eta\pi^+\pi^-)$	[1.944, 1.992]	[1.885, 1.933]	[2.004, 2.052]
$\pi^-\eta'(\rho\gamma)$	[1.944, 1.992]	[1.886, 1.930]	[2.002, 2.047]

B. Tag-candidate selection

Eight tag decay modes are used and listed in Table I, using the particle candidates selected according to Sec. III.A. In addition, there are several mode-specific criteria. For $D_s^- \to K^-K^+\pi^-$ and $D_s^- \to \pi^+\pi^-\pi^-$, the pion momenta are required to be greater than 0.1 GeV. For $D_s^- \to K^{\star-}\overline{K}^{\star 0}$, only the $(K_S^0\pi^-)(K^+\pi^-)$ channel is considered. The $K^{\star-}$ and $\overline{K}^{\star 0}$ candidate masses are required to be within 100 MeV of the nominal value [17]. For the $D_s^- \to \eta\rho^-(\rho^- \to \pi^-\pi^0)$, the ρ^- mass must be within 150 MeV of the nominal value [17]. For $D_s^- \to \pi^-\eta'(\eta' \to \rho\gamma), \rho^0 \to \pi^+\pi^-$, the η' mass must be within 20 MeV of the nominal value [17]. Furthermore, the $(\pi\text{-}\eta')$ helicity angle (defined as the angle θ_H, in the rest frame of the ρ, between the momentum of the π^- and the momentum of the D_s^-) is required to satisfy $|\cos\theta_H| < 0.8$.

The four-momentum of a tag candidate is defined by $(E_{tag}, \mathbf{p}_{tag})$, with the tag mass defined by $M_{\rm tag}$. The selection further makes use of the recoil mass $M_{\rm rec}$, defined as

$$M_{\rm rec} = \sqrt{(E_{\rm b} - E_{\rm tag})^2 - (\mathbf{p}_{\rm b} - \mathbf{p}_{\rm tag})^2}. \tag{2}$$

Here, $(E_{\rm b}, \mathbf{p}_{\rm b})$ is the four-momentum of the colliding beams. The $M_{\rm rec}$ distribution will peak only for those events where the photon is associated with the signal side, but even when the photon is associated with the tag side, $M_{\rm rec}$ is kinematically constrained so that $|M_{\rm rec} - M^\star| < 55$ MeV, where $M^\star$ is the nominal $D_s^\star$ mass [17]. Only candidates passing this selection are retained.

The main tag selection is obtained from a 2-D fit described below. Because of the complexity of the fit, the $M_{\rm tag}$ projection is fitted first, and the fit results used to constrain some of the final 2-D fit nuisance parameters. The $M_{\rm tag}$ projection is also best suited for side-band background subtraction.

The $M_{\rm tag}$ distribution is fitted with a double Gaussian function, G_2, multiplied by the fitted number of events, N, and a first degree polynomial, A_1, to describe signal and background

$$f(M_{\rm tag}) = NG_2(M_{\rm tag}) + A_1(M_{\rm tag}). \tag{3}$$

G_2 is a probability distribution composed of two Gaussian functions $G(x;\sigma,\mu)$, of unit area, peaking at μ and with width equal to σ. Here, the peak is set at $M_{\rm Ds}$, which is the nominal nominal D_s^+ mass [17], and the two Gaussians have fractional probabilities f_1 and $(1-f_1)$

$$G_2(M_{\rm tag}) = f_1 G(M_{\rm tag};\sigma_1, M_{\rm Ds}) + (1-f_1)G(M_{\rm tag};\sigma_2, M_{\rm Ds}). \tag{4}$$

The quantities σ_1 and σ_2 are fixed to the value obtained from the fit to the signal MC data. Having obtained f_1 from the fit, we construct the variable $\sigma_{12}^2 = f_1\sigma_1^2 + (1-f_1)\sigma_2^2$. The signal regions are required to be within $2.5\sigma_{12}$ from the peak position for each mode except for the $(\eta\rho)$ mode where it is selected within $2\sigma_{12}$.

The $M_{\rm tag}$ data fit results are listed in Table II. The rest of the peak fit parameters are listed in Table III. The $M_{\rm tag}$ distributions for the 8 modes are shown in Fig. 2. The sidebands in the $M_{\rm tag}$ distribution are listed, for each mode, in Table I.

Having determined the fit parameters for the $M_{\rm tag}$ distributions, a second kinematic constraint can be imposed using the MM^{*2} variable defined as

$$MM^{*2} = (E_{\rm b} - E_{\rm tag} - E_\gamma)^2 - (\mathbf{p}_{\rm b} - \mathbf{p}_{\rm tag} - \mathbf{p}_\gamma)^2, \tag{5}$$

where $(E_\gamma, \mathbf{p}_\gamma)$ is the photon four-momentum. If the final state is given by Eq. (1), MM^{*2} should peak at $M^2_{\rm Ds}$. The MM^{*2} mass selection criteria are found by a two-dimensional (2-D) binned likelihood fit in the $(MM^{*2}, M_{\rm tag})$ space. Each variable is also kinematically fitted, so that $M_{\rm tag}$ is the value obtained by constraining MM^{*2} to its nominal value, and vice versa. This procedure improves the signal and also minimizes any correlation between the two variables.

TABLE II. Number of D_s^- tag candidates $N_{\rm data}$ for each mode in the signal region and sidebands for the one-dimensional fit to $M_{\rm tag}$.

Modes	N_{data}	Low Sideband	High Sideband
$K^0_{\rm S}K^-$	5828 ± 92	1231	958
$K^+K^-\pi^-$	25990 ± 285	22385	19452
$K^{\star-}\overline{K}^{\star 0}$	2891 ± 100	2783	2647
$\pi^+\pi^-\pi^-$	8152 ± 369	56530	43475
$\eta\pi^-$	3635 ± 160	5727	3379
$\eta\rho^-$	6877 ± 330	26879	14658
$\pi^-\eta'(\eta\pi^+\pi^-)$	2344 ± 70	1040	572
$\pi^-\eta'(\rho\gamma)$	4451 ± 337	42412	25476

TABLE III. Signal peak parameters for each tag mode derived from $c\bar{c}$ MC simulation.

Mode	f_1	σ_1 (MeV)	σ_2 (MeV)
$K^0_{\rm S}K^-$	0.471	4.05	7.00
$K^+K^-\pi^-$	0.725	3.74	8.92
$K^{\star-}\overline{K}^{\star 0}$	0.771	3.43	10.65
$\pi^+\pi^-\pi^-$	0.899	4.84	9.88
$\eta\pi^-$	0.650	9.85	15.56
$\eta\rho^-$	0.574	10.8	18.3
$\pi^-\eta'(\eta\pi^+\pi^-)$	0.590	5.71	13.34
$\pi^-\eta'(\rho\gamma)$	-	9.60	-

The 2-D fit is done for each mode separately, and its purpose is to extract the final number of tags for each mode, N_i, while building on the information obtained in the one-dimensional $M_{\rm tag}$ fit. The fitting function is

$$f(M_{\rm tag}, MM^{*2}) = N_i G_2(M_{\rm tag})C(MM^{*2}) + G_2(M_{\rm tag})A_5(MM^{*2}) + A_1(M_{\rm tag})A_5(MM^{*2}). \quad (6)$$

For each mode, the signal is described by the product of a double Gaussian in the $M_{\rm tag}$ projection, defined in Eq. (4) and Crystal Ball function [23], defined as C in the equations, in the MM^{*2} projection, respectively. One of the background components is the combination of a real tag with a random γ. This type of background (BG_1 in Fig. 3 below, and the second term in Eq. (6)) is described by the same double Gaussian $G_2(M_{\rm tag})$ and a 5th degree

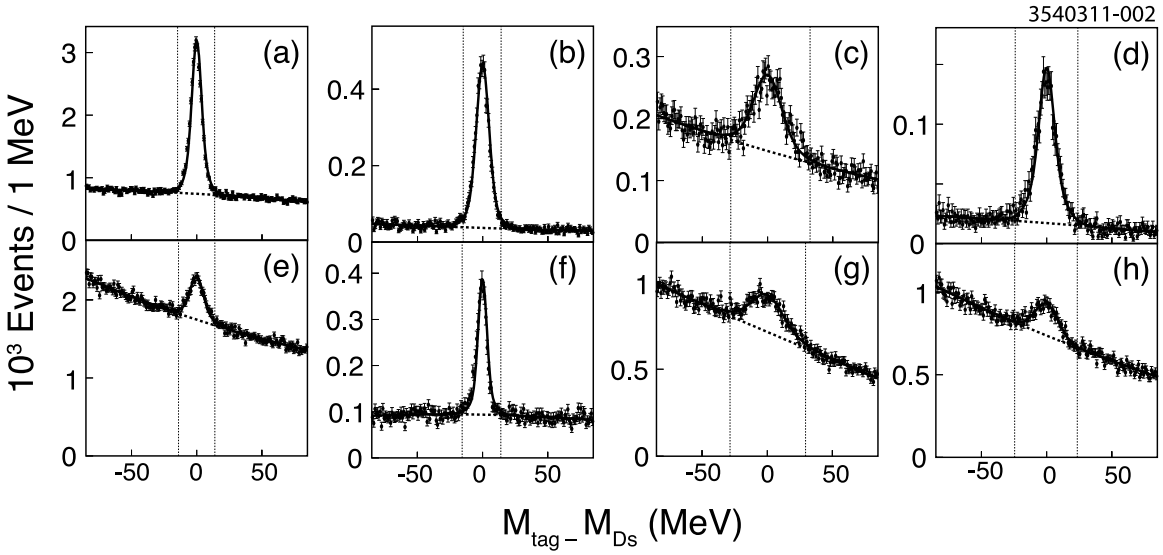

FIG. 2. Distribution of $M_{\rm tag} - M_{\rm Ds}$ of $D_{\rm s}^-$ candidates, for the different tags: (a) $K^+K^-\pi^-$; (b) $K^0_{\rm S}K^-$; (c) $\eta\pi^-$; (d) $\pi^-\eta'(\eta\pi^+\pi^-)$; (e) $\pi^+\pi^-\pi^-$; (f) $K^{\star-}\overline{K}^{\star 0}$; (g) $\eta\rho^-$, and (h) $\pi^-\eta'(\rho\gamma)$. The fitted background A_1, described in the text, is indicated by the dashed-dotted slope. The signal mass region is indicated by the vertical dotted lines.

polynomial $A_5(MM^{*2})$. The other background (BG_2 in Fig. 3 below, and the third term in Eq. (6)) is due to fake tags. The PDF here is the product of a 1st order polynomial ($M_{\rm tag}$) and a 5th order polynomial (MM^{*2}). To simplify the fit, the $M_{\rm tag}$ projections are fitted using the signal function obtained in the 1-D $M_{\rm tag}$ fit, but the background parameters are varied.

TABLE IV. MM^{*2} selection range and the number of tags in each mode obtained from the two-dimensional fit. Total number of tags, $N_{\rm tag}$ is also given. The quoted error is statistical only.

Modes	Lower limit (GeV^2)	Upper limit (GeV^2)	N_i(data)
$K^0_{\rm s}K^-$	3.7876	3.9539	3442 ± 138
$K^+K^-\pi^-$	3.7939	3.9510	15647 ± 271
$K^{\star-}\overline{K}^{\star 0}$	3.7505	3.9847	1707 ± 94
$\pi^+\pi^-\pi^-$	3.7701	3.9633	4595 ± 298
$\eta\pi^-$	3.7662	3.9798	2355 ± 187
$\eta\rho^-$	3.7698	3.9632	3606 ± 640
$\pi^-\eta'(\eta\pi^+\pi^-)$	3.7409	3.9888	1716 ± 142
$\pi^-\eta'(\rho\gamma)$	3.7875	3.9601	3373 ± 240
$N_{\rm tag}$	-	-	36441 ± 852

The MM^{*2} distributions are shown in Fig. 3. The MM^{*2} signal regions for each mode are chosen so as to have 95% signal efficiency. The MM^{*2} selection is summarised in Table IV. Table IV also lists the final number of tags obtained in each tag mode, N_i, as well as the total number of tags, $N_{\rm tag}$, used to extract the final result.

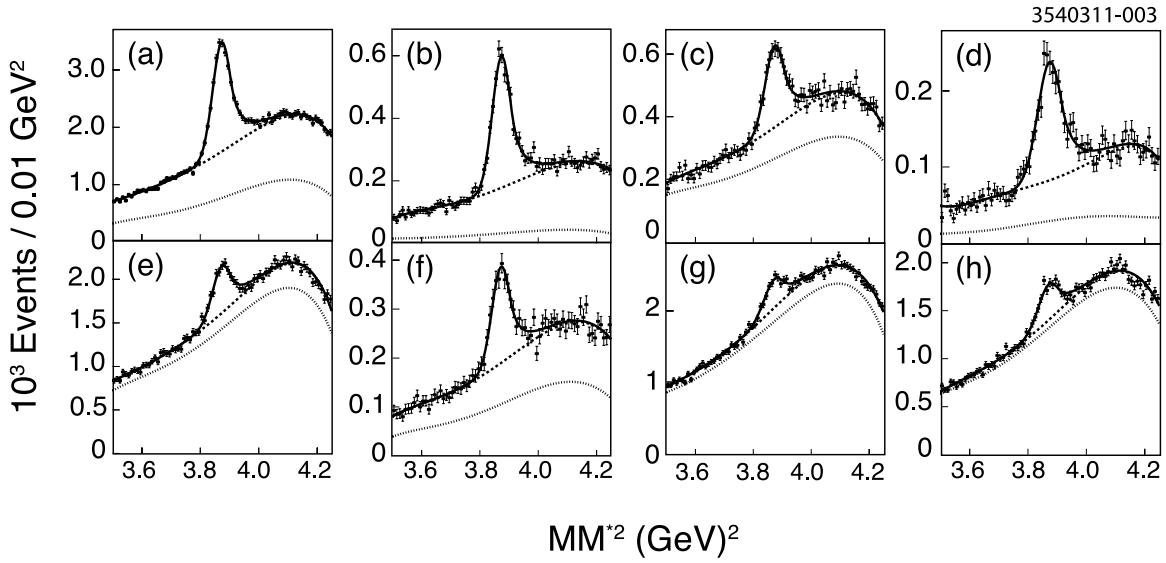

FIG. 3. MM^{*2} distributions for the 8 tag modes. Dash-dotted lines are the BG_2 background described in the text. Dashed lines are total background $BG_1 + BG_2$. (a) $K^+K^-\pi^-$; (b) $K^0_S K^-$; (c) $\eta\pi^-$; (d) $\pi^-\eta'(\eta\pi^+\pi^-)$; (e) $\pi^+\pi^-\pi^-$; (f) $K^{\star-}\overline{K}^{\star 0}$; (g) $\eta\rho^-$, and (h) $\pi^-\eta'(\rho\gamma)$.

C. Signal selection

The signal is selected by requiring one positron candidate, of charge opposite to the tag charge, two charged pion candidates, of opposite charge, no extra good tracks, and a good π^0, all selected exclusively of the objects used in the tag. The selection requires a specific number of tracks, and multiple candidates can arise only due to multiple π^0 candidates. In case of multiple candidates, the π^0 is selected as follows. Given the photon-photon mass $M_{\gamma\gamma}$, and the calculated mass error $\sigma_{\gamma\gamma}$, the one with the lowest $\chi^2 = [(M_{\gamma\gamma} - M_{\pi^0})/\sigma_{\gamma\gamma}]^2$ is chosen. Additional candidate photons are ignored.

The positron, charged pions, and π^0 are added together to form the four-vector $(E_{\rm s}, \mathbf{p}_{\rm s})$. The measured neutrino candidate mass squared, MM^2, is defined as

$$MM^2 = (E_{\rm b} - E_{\rm tag} - E_\gamma - E_{\rm s})^2 - (\mathbf{p}_{\rm b} - \mathbf{p}_{\rm tag} - \mathbf{p}_\gamma - \mathbf{p}_{\rm s})^2.$$

The MM^2 distributions, with $M_{\rm tag}$ sideband subtraction, of the two control samples $\eta e^+\nu$ and $\phi e^+\nu$ are shown in Fig. 4. Based on the shape of MM^2, events with -0.05 GeV^2 $<$ MM^2 < 0.05 GeV^2 are selected for the final analysis.

The mass of the $\pi^+\pi^-\pi^0$ combination M_3 was not used in the candidate selection, and provides the spectrum that is fitted to extract the final result. In Fig. 5, the M_3 spectrum is presented, including $M_{\rm tag}$ sideband contributions. Two peaks are clearly present, at the η and ϕ masses, with no sign of a signal in the ω mass region.

The M_3 peaks in the signal MC samples are fitted to a Breit-Wigner shape (indicated as BW in the equations), convoluted with a double Gaussian,

$$s(x) = K \int BW(x_1) G_2(x - x_1) dx_1, \tag{7}$$

where K is a normalization constant to give $s(x)$ a unit area. Table V lists the fit results for each of the signal MC samples generated for this analysis.

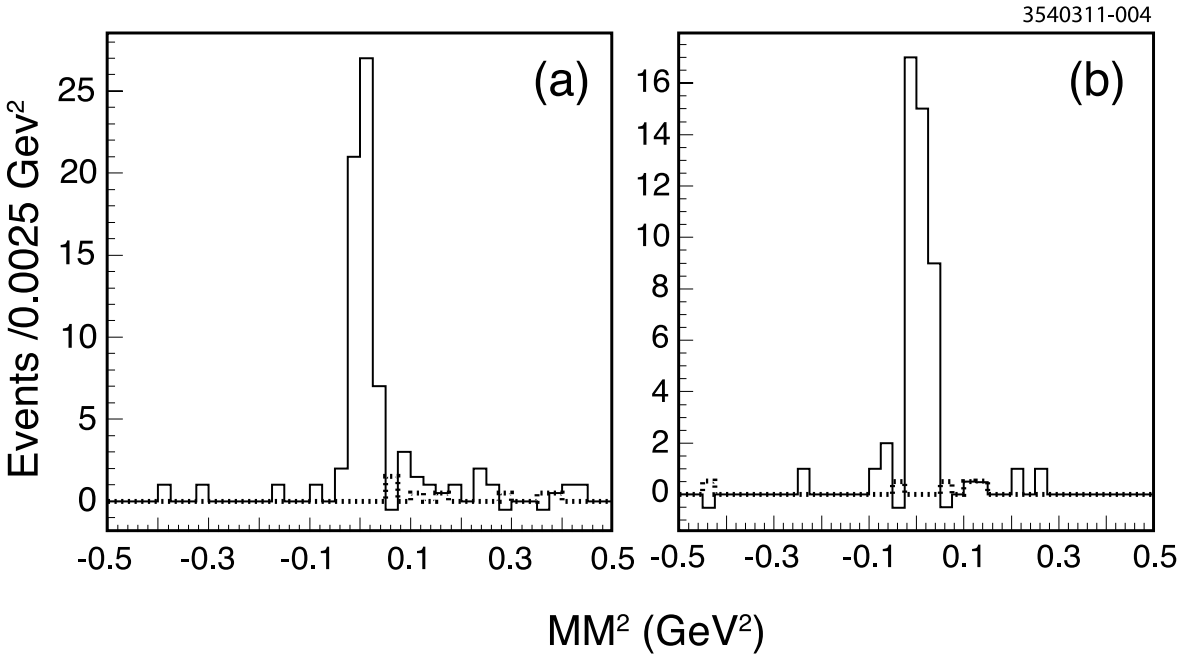

FIG. 4. Control sample MM^2 distributions. (a) solid, $D_s^+ \to \eta e^+\nu$ distribution after $M_{\rm tag}$ sideband subtraction, and $M_{\rm tag}$ sideband distribution (dotted). (b) solid, $D_s^+ \to \eta e^+\nu$ distribution after $M_{\rm tag}$ sideband subtraction, and $M_{\rm tag}$ sideband distribution (dotted).

TABLE V. M_3 signal peak parameters evaluated from signal MC sample. All quantities are defined in the text.

Decay	f_1	σ_1 (MeV)	σ_2 (MeV)	R.M.S. (MeV)
$\eta e^+\nu$	0.8844	3.165	19.85	7.37
$\omega e^+\nu$	0.8783	5.500	22.52	9.40
$\phi e^+\nu$	0.8361	5.940	19.83	9.73

The reconstruction efficiency ϵ for the $\omega e^+\nu$ final state is computed by applying the same requirements to the signal MC events, but correcting for the number of tags found in the data,

$$\epsilon = \frac{1}{N_{\rm tag}} \Sigma N_i \epsilon_i, \tag{8}$$

ϵ_i being the signal MC efficiency for mode i. The result is $\epsilon = (5.11 \pm 0.15)\%$, with the error due to MC statistics.

IV. FINAL FIT

Figure 6 shows only the M_3 region used in the fit, which contains $N_{\rm obs} = 18$ events. The $\Delta_{M3} = 250$ MeV mass window is centered at the nominal ω mass [17]. In the Fig. 6(a), the

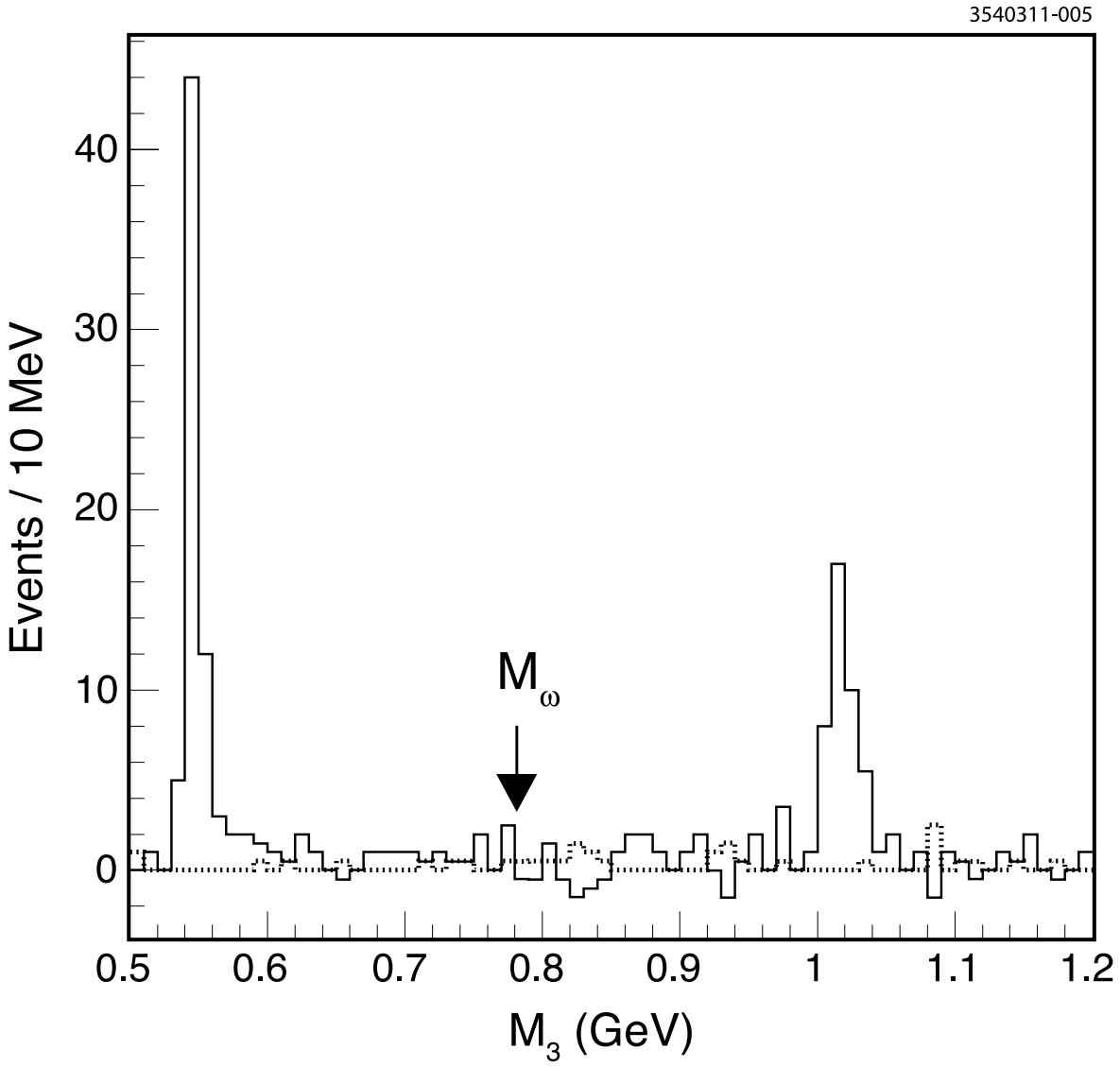

FIG. 5. M_3 distribution. Solid: signal selection, after $M_{\rm tag}$ sideband subtraction. Dotted: $M_{\rm tag}$ sideband contribution. The arrow shows the location of the ω nominal mass, Ref. [17].

data distribution and the fit to the data (described below) are shown. In Fig. 6(b), the MC distribution is shown.

Three potential sources of background are considered: non-$D_{\rm s}$ backgrounds, $D_{\rm s}$ backgrounds where there are non-resonant final states (which have not yet been observed, and are not present in the MC simulation), and backgrounds where there is a true ω. $M_{\rm tag}$ sideband subtraction only subtracts the first source. A direct fit of a signal and a background component subtracts the first two. The third source of background is subtracted via MC simulation, and is discussed below. The signal yield is determined by a one parameter unbinned likelihood fit [17]. The free parameter is the total number of signal events S. The background level is constrained by the normalization of the probability. S is multiplied by a function of unit area $s(x)$, Eq. (7). The final expression of the unbinned likelihood,

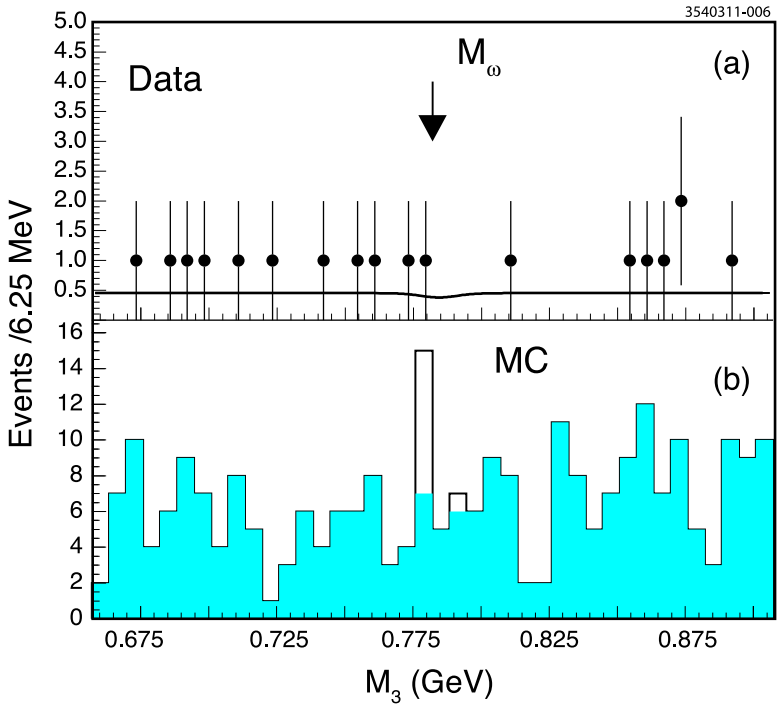

FIG. 6. M_3 distribution in the 250 MeV wide region centered at the nominal ω mass. No $M_{\rm tag}$ sideband subtraction was used. (a) comparison of data (points) and best fit according to Eq. (9) (line). (b) The MC sample, normalized to 20 times the data statistics. Solid: non-resonant backgrounds. Empty: resonant backgrounds. The arrow shows the location of the ω nominal mass.

$L_u = \Pi_i P_i$, is obtained from the probabilities

$$P(M_{3i}|S) = P_i = (S/N_{\rm obs})s(M_{3i}) + (1 - S/N_{\rm obs})/\Delta_{M3}, \tag{9}$$

which correspond to a signal S, distributed according to $s(M_3)$, plus a flat background.

Figure 7 shows the likelihoods obtained for data, without any peaking background subtraction, in the $S > 0$ region. The 90% confidence level (C.L.) is calculated using only the $S > 0$ portion of the likelihood. The statistical only upper limit on S at the 90% C.L. is $S_{90} = 3.78$ events.

Unbinned likelihood fits, in one dimension, can be tested for goodness of fit using the Cramer-Von Mises test [24], where the goodness of fit parameter is

$$G = \int_{M_3^{\rm min}}^{M_3^{\rm max}} [F(M_3) - F_N(M_3)]^2 dF(M_3). \tag{10}$$

The integral limits are the limits of the fit interval. $F(M_3)$ is the integrated probability function for best-fit parameters,

$$F(M_3) = \int_{M_3^{\rm min}}^{M_3} P(M_3', S_{\rm max}) dM_3'. \tag{11}$$

Here $S_{\rm max} = 0$, so that F is in fact a straight line. One has $F = (M_3 - M_3^{\rm min})/\Delta_{M_3}$ and $dF(M_3) = dM_3/\Delta_{M_3}$. F_N is a step function such that $F_N(M_3) = N/N_{\rm obs}$, where N is the rank of the largest event mass which is less than M_3. The two functions are shown in Fig. 8.

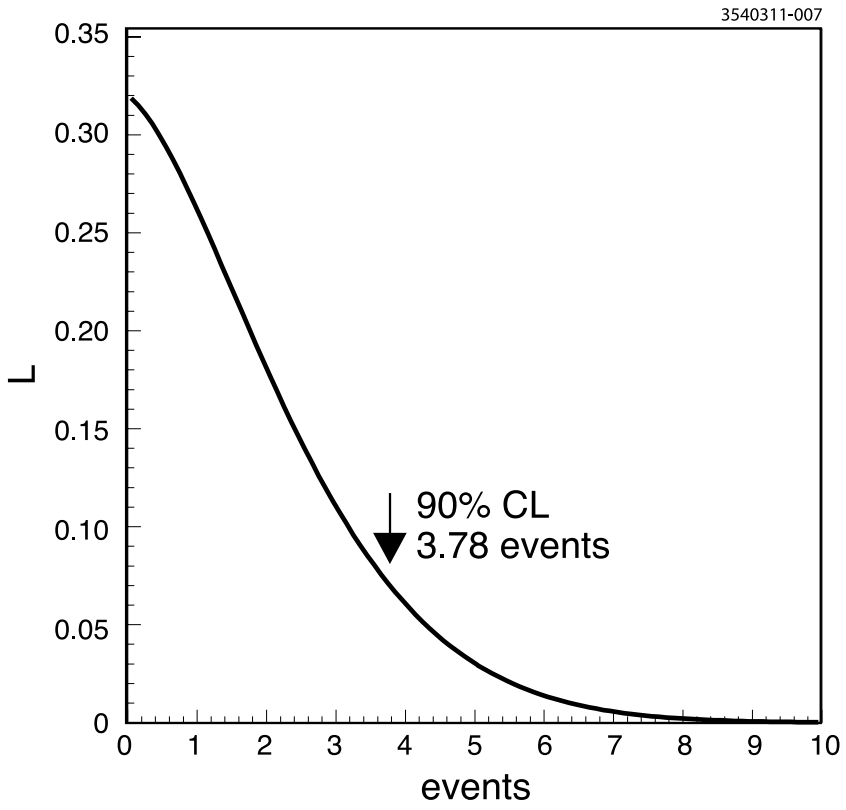

FIG. 7. Statistical only likelihood, normalized to unit area over the positive signal region, for the observed number of signal events in data. The 90% C.L. was computed using only the positive signal region.

A toy MC program was run to generate an ensemble of 10^5 unbiased experiments. Figure 8 shows the distribution of G for the ensemble, also shown is the value of G obtained in the fit to data. Only 13.1% of the fits to the generated experiments are better than that to the data. The toy MC program also made it easy to apply the Kolmogorov-Smirnov (KS) test, which simply computes the maximal difference between F and F_N. Only 16.0% of the unbiased experiments produced a better KS test than the data. The fit to the data is excellent.

V. DETERMINATION OF BRANCHING FRACTION AND SYSTEMATIC ERRORS

The statistical upper limit on the number of events is translated into a statistical only limit on the branching fraction $\mathcal{B}_{90}$ according to the following equation

$$\mathcal{B}_{90} = \frac{S_{90}}{\epsilon N_{\rm tag}}. \tag{12}$$

There are three quantities on the right hand side of Eq. (12), with central values $S_{90} = 3.78$, $\epsilon = 0.0511$ and $N_{\rm tag} = 36441$, yielding $\mathcal{B}_{90} = 0.203\%$, which is a purely statistical

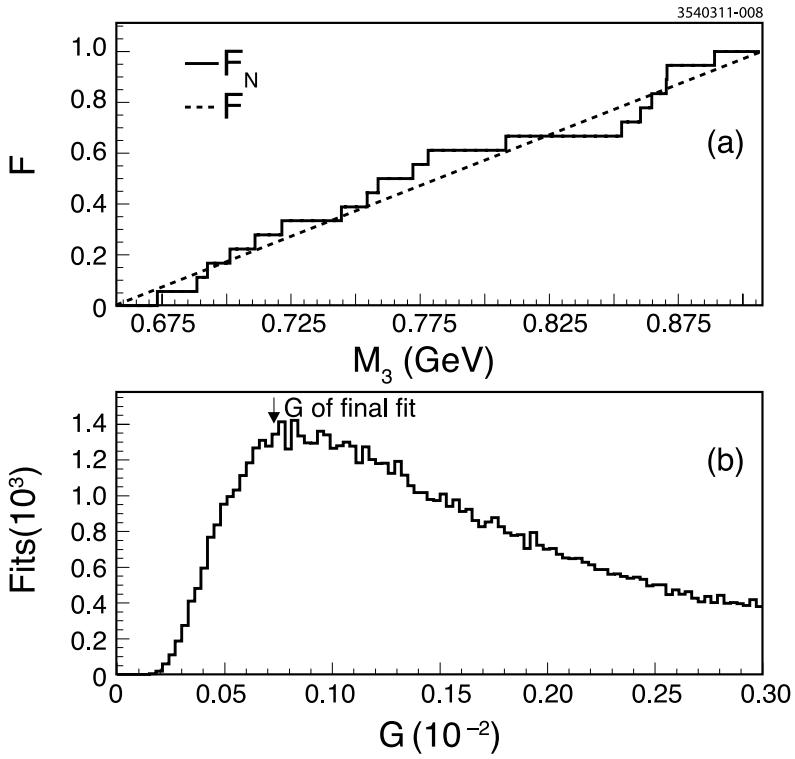

FIG. 8. Cramer-Von Mises test of goodness of fit, for the final fit of this analysis. (a) Comparison of the integrated probability distribution F (dashed) and the step function F_N described in the text (solid). (b) Comparison of the G obtained in this analysis, with a distribution obtained from 10^5 unbiased toy MC fits.

limit. $N_{\rm tag}$ has a statistical error of its own, and each of the three quantities in Eq. (12) has systematic errors which are discussed below.

A. Systematic errors

Table VI, first row, contains the relevant parameters of the unbinned likelihood (Fig. 7), in the form $\mu \pm \sigma$. μ is the S value for which L_u is maximal, if one allows also $S < 0$ values. It describes the form of the likelihood, but is not used in the determination of the final result.

Systematic errors to S_{90} are also listed in Table VI. The error associated with the assumed mass and width of ω is estimated by varying the central values by the uncertainties given in Ref. [17].

The greatest source of S_{90} systematic errors is related to irreducible backgrounds. These also shift the location of the likelihood peak to lower values. Fig. 6 shows the background distribution by physical source. All but one of the true ω are due to the decay chain $D_s^+ \to \eta' e^+ \nu$ with $[\mathcal{B} = (1.12 \pm 0.35)\%]$, followed by $\eta' \to \omega\gamma$, with $[\mathcal{B} = (3.02 \pm 0.33)\%]$ [17]. A dedicated MC simulation for this channel generated 5000 events of which 51 passed all selections. This corresponds to an irreducible background of (0.53 ± 0.19) events. Note that the largest source of error is the semileptonic $\mathcal{B}$ error from Ref. [17]. Therefore, this source

of systematics can not be significantly improved with increased simulation statistics.

A second irreducible background comes from $D_s \to \omega X$ events. Zero events are found in the MC events from the direct decay $D_s^+ \to \omega\pi^+$. The $c\bar{c}$ MC significantly underestimates the $(D_s \to \omega X)$ yield, which is 0.6% in the $c\bar{c}$ MC but 6.1% in data [25]. The decay $D_s^+ \to \omega\pi^+$ is in the $c\bar{c}$ MC, but no other $\omega n(\pi)$ decays. A dedicated MC for $D_s^+ \to \omega\pi^+\pi^0$, which was assumed to saturate the 5.5% difference, was run, and zero events were found. The probability for n background events, given zero MC candidates, is exponential in shape. The systematic error from this source can be represented as (0.02 ± 0.02) in Table VI.

There was one more true ω event which is in the continuum MC sample, corresponding to one more irreducible background of 0.15 ± 0.15 events.

TABLE VI. Summary of statistical and systematic errors of S_{90}. The first block is the statistical error from the experiment. The second block are errors associated with the quantity S_{90} of Eq. (12) and consists of uncertainties due to the mass and width of the omega, and errors in estimating three irreducible backgrounds as described in the text. The last block are percentage systematic errors associated with $N_{\rm tag}$ or ϵ.

Type	Cent. val. (evts.)	σ (evts.)
Data fit	-0.25	2.21
ω mass	–	0.04
ω width	–	0.006
$D_s^+ \to \eta' e^+ \nu$	-0.53	0.19
$D_s^+ \to \omega X$	-0.02	0.02
Continuum	-0.15	0.15
Type	Cent. val.(%)	σ (%)
$N_{\rm tag}$ stat.	–	2.3
$N_{\rm tag}$ syst.	–	2.0
MC statistics	–	2.7
$\mathcal{B}(\omega \to 3\pi)$	–	0.8
Tracking	–	0.9
π^0 eff.	–	1.0
π^0 selection variation	–	0.5
Positron eff.	–	0.6
MC form factor	–	0.5
Extra track selection	–	0.04
Particle ID	–	0.1

$N_{\rm tag}$ was obtained through a fit, with a statistical error of 2.3%. Systematic errors can enter the analysis only through the bias in the choice of fitting function. This can be quantified by varying the fitting function. For each tag mode, the fitting function for the signal was changed, first term of Eq. (6). The Crystal Ball function was varied in two ways, by keeping the n parameter fixed to its MC fitted values and by changing the (n, α) parameters by one σ in a mode specific way. The background was also varied. Instead of a fifth degree polynomial, the data were fitted with a fourth and a sixth degree polynomial. The background was also changed by fixing the amount of BG_1 background (described in

Sec. III.B) to one standard deviation above or below its central value. Variations of $N_{\rm tag}$ due to changes in the fitting function were as low as -1.8% and as high as $+1.5\%$. The assigned systematic $N_{\rm tag}$ error is 2.0%.

Correlations may affect the fit of the $(M_{\rm tag}, MM^{*2})$ peak, because the fit assumes the two variables are not correlated. To study this, we have computed the $(M_{\rm tag}, MM^{*2})$ correlation coefficient in the signal MC sample, by calculating the correlation coefficient in each tag mode, and then reweighting for the observed number of events in each mode. The result is $\rho = (-1.6 \pm 0.9)\%$. The fit error due to remnant correlations is of order ρ^2 and is neglected.

Finally, there are the systematic uncertainties on the efficiency to be considered. The ω branching fraction uncertainty is 0.8% [17]. The tracking efficiency error is a 0.3% Gaussian systematic error per signal track, to be added linearly, totaling 0.9% per event [26].

The π^0 reconstruction efficiency error is 1% [27], but depends on the exact selection criteria. To estimate the size of the systematics induced by changing selection criteria, the signal MC sample with and without the energy and angular criteria which were used to select photon candidates. There were 41269 reconstructed events with the criteria, and 41868 without the criteria, a difference of 1.5%. There were 101 events instead of 99 in the combined η and ϕ peaks, a difference of 2%. We assumed a further 0.5% systematic error, listed in Table VI.

The positron reconstruction efficiency is evaluated in a manner similar to Ref. [27]. Positron efficiencies have been investigated by the Collaboration using a variety of well-known kinematically constrained QED processes. The experimentally measured corrections are convoluted with the positron momentum distribution to obtain the efficiency uncertainty, which is 0.6%. The effects of the extra track cuts and of particle ID cuts can be estimated from the MC sample, by varying or eliminating the cuts. We find errors of 0.04% and 0.1% for the extra track cut and particle ID cuts respectively.

Finally, a different form factor will change the efficiency, mostly because events with low q^2 (the positron-neutrino mass) produce lower energy positrons. The signal MC produce phase-space distributed events, and therefore a constant form factor. To evaluate this source of systematics, the form factor was varied by $\pm 20\%$, by reweighting the signal MC events according to the weights

$$w_{\pm i}(q_i^2) = 1 \pm \frac{0.2(q_i^2 - < q^2 >)}{< q^2 >},$$

with $< q^2 >$ being the mean q^2 in the signal MC sample. The new efficiencies are 5.08% and 5.14% respectively, to be compared to the given value of 5.11%. A systematic error of 0.5% is assigned to this systematics.

B. Determination of the branching fraction

To obtain the final result, Gaussian and non-Gaussian errors are convoluted with the non-Gaussian signal S distribution given by the likelihood (Fig. 7), by means of a toy MC program. The procedure is used for several reasons. First, the main source of error, the unbinned likelihood, is non-Gaussian, whereas the smaller sources of error are mostly Gaussian. Second, some sources of error shift the central value of the likelihood, an effect which can be treated exactly by shifting the likelihood on an event-by-event basis. Finally, the exponential and correlated nature of some of the error sources can be reproduced exactly by MC simulation.

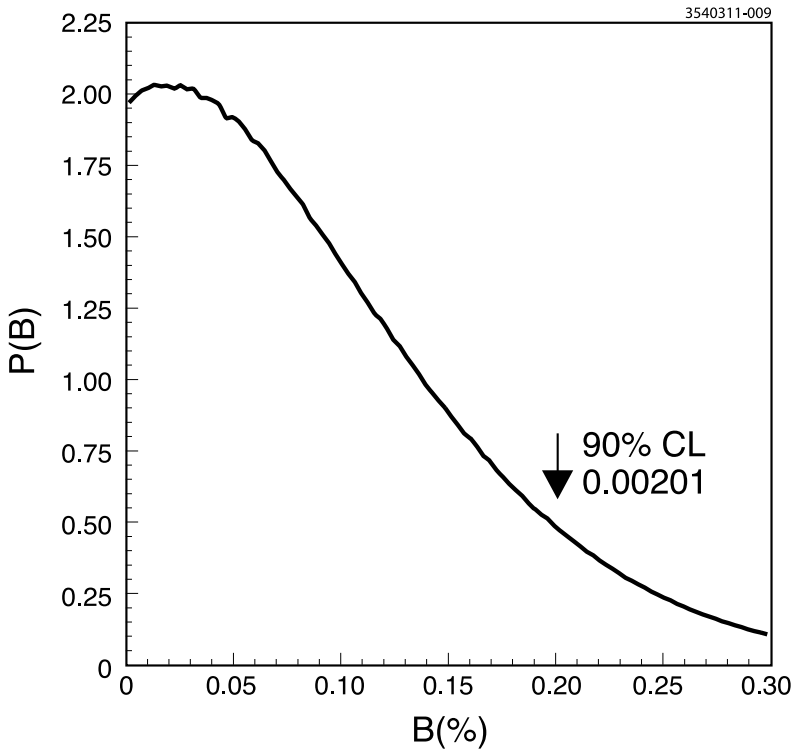

FIG. 9. Final probability distribution for the branching fraction, after convolution of all statistical and systematic errors, as described in the text.

A total of 25×10^6 toy experiments are generated, to obtain the probability distribution in Fig. 9. The cumulative effect of the systematic errors is to increase the limit, and the cumulative effect of the irreducible backgrounds is to decrease the limit. Taking into account the systematic uncertainties and the irreducible backgrounds, the upper limit on the branching fraction changes from 0.203% (statistical only) to 0.201%.

VI. CONCLUSION

We report the first measurement of an upper limit for the branching fraction $\mathcal{B}(D_s^+ \to \omega e^+ \nu)$. We find $\mathcal{B}(D_s^+ \to \omega e^+ \nu)$ <0.20% at the 90% C.L., which does not exclude that expected from the model of Ref. [16].

ACKNOWLEDGMENTS

We gratefully acknowledge the effort of the CESR staff in providing us with excellent luminosity and running conditions. D. Cronin-Hennessy thanks the A.P. Sloan Foundation. This work was supported by the National Science Foundation, the U.S. Department of Energy, the Natural Sciences and Engineering Research Council of Canada, and the U.K.

Science and Technology Facilities Council.

---

[1] S. K. Choi *et al.* (Belle Collaboration), Phys. Rev. Lett. **91**, 262001 (2003).
[2] K. Abe *et al.* (Belle Collaboration), Phys. Rev. Lett. **98**, 082001 (2007).
[3] B. Aubert *et al.* (BABAR Collaboration), Phys. Rev. D **73**, 011101 (2006).
[4] Q. He *et al.* (CLEO Collaboration), Phys. Rev. D **74**, 091104 (2006).
[5] F. E. Close and P. R. Page, Phys. Lett. B **578**, 219 (2003).
[6] M. B. Voloshin, Phys. Lett. B **579**, 316 (2004).
[7] N. A. Tornqvist, Phys. Lett. B **590**, 209 (2004).
[8] E. S. Swanson, Phys. Lett. B **588**, 189 (2004).
[9] E. Braaten and M. Kusunoki, Phys. Rev. D **69**, 114012 (2004).
[10] C. Y. Wong, Phys. Rev. C **69**, 055202 (2004).
[11] I. Bigi *et al.*, Phys. Rev. D **72**, 114016 (2005).
[12] L. Maiani *et al.*, Phys. Rev. D **72**, 031502 (2005).
[13] T. W. Chiu *et al.* (TWQCD Collaboration), Phys. Lett. **646**, 95 (2007).
[14] G. Bonvicini, in *Transition from low to high Q form factors*, Proceedings from the TJNAF Workshop, edited by G. Strobel and D. Mack, (University of Georgia, Athens, 1999).
[15] F. Gabbiani, J. Qiu, and G. Valencia, Phys. Rev. D **66**, 114015 (2002).
[16] M. Gronau and J. Rosner, Phys. Rev. D **79**, 074006 (2009).
[17] K. Nakamura *et al.* (Particle Data Group), J. Phys. G **37**, 075021 (2010).
[18] D. Cronin-Hennessy *et al.* (CLEO Collaboration), Phys. Rev. D **80**, 072001 (2009).
[19] Y. Kubota *et al.* (CLEO Collaboration), Nucl. Instrum. Methods A **320**, 66 (1992); D. Peterson *et al.*, Nucl. Instrum. Methods A **478**, 142 (2002); M. Artuso *et al.*, Nucl. Instrum. Methods A **554**, (2007).
[20] D. Lange *et al.*, Nucl. Instrum. Methods A **462**, 152 (2001).
[21] R. Brun *et al.*, `GEANT 3.21`, CERN Program Library Long Writeup W5013, unpublished.
[22] S. Dobbs *et al.* (CLEO Collaboration), Phys. Rev. D **76**, 111201 (2007).
[23] M. J. Oreglia, Ph.D Thesis, SLAC-236 (1980), J. E. Gaiser, Ph.D. Thesis, SLAC-255 (1982).
[24] T. W. Anderson, Ann. Math. Statist. **33**, 1148 (1962).
[25] J. Y. Ge *et al.* (CLEO Collaboration), Phys. Rev. D **80**, 051102 (2009).
[26] P. Naik *et al.* (CLEO Collaboration), Phys. Rev. D **80**, 112004 (2009).
[27] S. Dobbs *et al.* (CLEO Collaboration), Phys. Rev. D **77**, 112005 (2008).